

Lava planets interior dynamics govern the long-term evolution of their magma oceans

Charles-Édouard Boukaré^{1*}, Daphné Lemasquerier², Nicolas B. Cowan^{4,1}, Henri Samuel¹ and James Badro¹

^{1*}Université Paris Cité, Institut de physique du globe de Paris, CNRS, 1, rue Jussieu, Paris, 75005, France.

^{2*}University of St. Andrews, School of Mathematics and Statistics, North Haugh, St Andrews, KY16 9SS, UK.

^{4*}Department of Earth and Planetary Sciences, McGill University, 3450, rue University, Montréal, H3A0E8, Canada.

^{5*}Department of Physics, McGill University, 3450, rue University, Montréal, H3A0E8, Canada.

*Corresponding author(s). E-mail(s): boukare@ipgp.fr;
 Contributing authors: d.lemasquerier@st-andrews.ac.uk;
nicolas.cowan@mcgill.ca; badro@ipgp.fr; samuel@ipgp.fr;

Abstract

Lava planets are rocky exoplanets that orbit so close to their host star that their day-side is hot enough to melt silicate rock. Their short orbital periods ensure that lava planets are tidally locked into synchronous rotation, with permanent day and night hemispheres. Such asymmetric magma oceans have no analogs in the Solar System and will exhibit novel fluid dynamics. Here we report numerical simulations of lava planet interiors showing that solid-liquid fractionation in the planetary interior has a major impact on the compositional structure and evolution of the planet. We explored two styles of dynamics that depend primarily on the interior thermal state : 1) a hot fully molten interior, and 2) a mostly solid interior with a shallow day-side magma ocean. In the hot interior scenario, the atmosphere reflects the planet's bulk silicate composition and the night-side crust is gravitationally unstable and constantly replenished. In the cool interior scenario, the distilled atmosphere will lack Na, K and FeO, and the night-side mantle is entirely

2 *Lava Planets Interior Dynamics*

solid, with a cold surface. These two end-member cases can be distinguished with observations from the James Webb Space Telescope, offering an avenue to probe the diversity of terrestrial exoplanet evolutions.

Keywords: Exoplanets, Magma Oceans, Rocky Planets Formation and Evolution, Atmosphere-interior interaction.

Astronomers have recently discovered a new class of exoplanets that offer a unique window into rocky interiors: lava planets [1–8]. These planets have densities consistent with Earth-like bulk composition but orbit so close to their star, that they are expected to have lost all their volatiles to space [9]. Due to the tremendous tidal forces at these distances, lava planets should be tidally locked into synchronous rotation. Tidal dissipation may be an important source of heat in lava planet. Their 2000–3000 K day-sides support an atmosphere of vaporized silicate rocks [10–12] which may be observable with the James Webb Space Telescope (JWST) [13–16]. The composition of such an atmosphere is determined by that of the underlying magma ocean, which is intimately linked to the dynamics of molten and solid mantle.

Hemispherical magma oceans on lava planets challenge standard models of terrestrial interior dynamics. A pioneering geodynamic study investigated the role of day-side heating on tidally locked super-Earths [17]. However, this work considered stellar flux in the range of 1000 W m^{-2} , orders of magnitude too low to allow for melting of silicate rocks on the day-side surface. Scaling laws have been used to predict first order aspects of lava planet dynamics with a day-side magma ocean [12]. Lava planet models [11, 12, 18, 19] recognized the primary role of the long-term evolution of the rocky solid interior on the hemispherical magma oceans as well as on their observable atmosphere. However, the internal dynamics of lava planets remain unexplored and poorly understood.

Here, we numerically model the interior dynamics of lava planets using two complementary codes to investigate (1) the solid-liquid multiphase fluid dynamics, (2) and the roles of spherical geometry, turbulence and rotation (see Methods). The motivation is that if the viscosity of the magma ocean is sufficiently small, turbulence and rotation could play a role in its dynamics, as suggested for the early Earth’s magma ocean [20–22]. The surface temperature is dictated by radiative equilibrium because plausible atmospheres are optically thin [11, 12, 14]. We use the surface temperature gradient for the specific lava planet K2-141b accounting for the finite angular size of the star as seen from the planet, which means that more than half the planet is illuminated [14]. We adopted the radius of K2-141b ($1.5 R_{\oplus}$) and assume that the Core–Mantle Boundary (CMB) is located halfway between the center of the planet and its surface.

We describe the internal dynamics of a lava planet chronologically from an initially hot and molten state [20, 23, 24] to the steady state stage when the mantle is completely solid, except for a shallow day-side magma ocean [12]. We identify three regimes: the global magma ocean, the mushy ocean, and the solid-state mantle.

Our 3D simulations show that the interior temperature in the global magma ocean regime is homogenized by turbulent convective currents, although there remains a clear distinction between a colder and warmer hemisphere (Fig. 1a). In our 2D simulations allowing for phase changes, however, the temperature is buffered by the melting curve of silicates and the homogenization is even more thorough (Fig. 1b). In both 2D and 3D simulations, the imposed surface

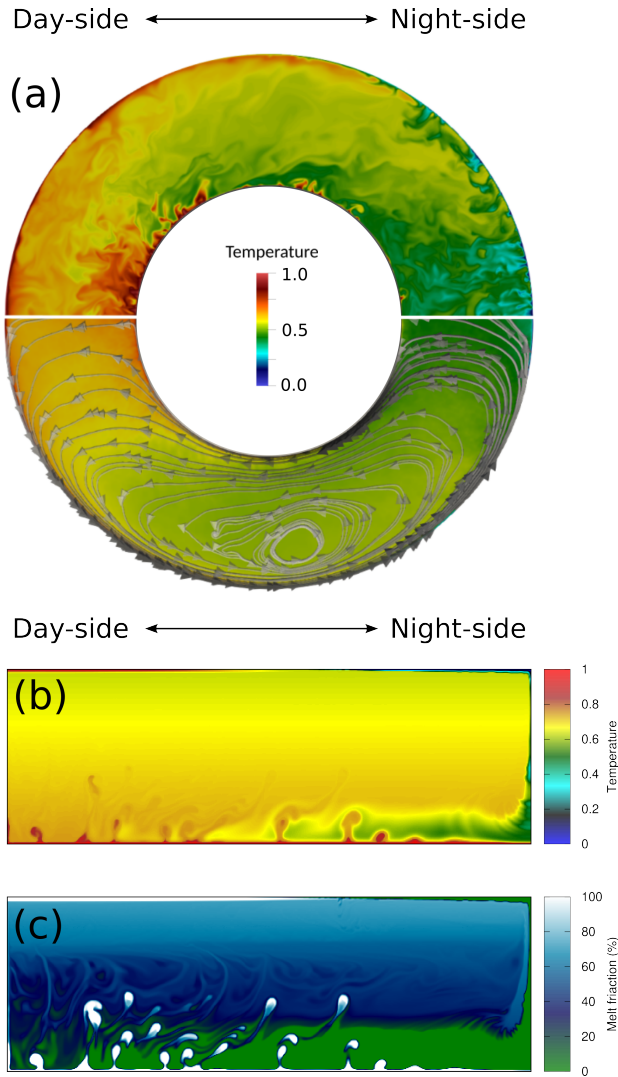


Fig. 1 Numerical simulations of lava planets interior dynamics with no rotation. The temperature scale is the maximum super-adiabatic temperature contrast: temperature is 1 at the base of the magma ocean, 0 at the surface on the night-side and 1 at the surface on the day-side. (a) Equatorial slices from the turbulent model in spherical geometry with no phase change: the upper half is a snapshot and the lower half is a time average over 12 turbulent turnover times with superposed streamlines. (b and c) Temperature and melt fraction from the 2D Cartesian model that accounts for phase change. 2D and 3D simulations show that lava planet interior dynamics is governed by both horizontal convection driven by temperature gradients at the surface imposed by stellar radiation, and vertical convection due to the temperature difference between the surface and the iron core. With solid-liquid phase change, the temperature is buffered by the silicates melting curve in partially molten regions.

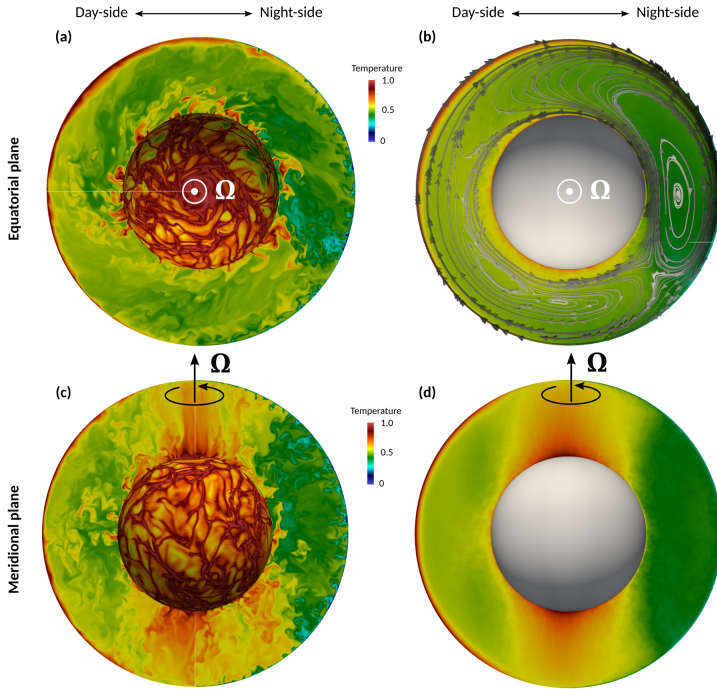


Fig. 2 3D simulations of the turbulent ocean dynamics in the fully-molten, low-viscosity case with rotation. Left: snapshots. Right: Time average over 14 turbulent turnover times. (a,b) Equatorial slices. (c,d) Meridional slices. Rotation produces a longitudinal shift of downwelling and upwelling regions with respect to the anti-stellar and sub-stellar points. An asymmetry between the western and eastern hemispheres also develops in the bulk of the ocean.

temperature gradient generates a global circulation, with downwellings on the night-side and a global return flow on the day-side (Fig. 1a, see also Supplementary Fig. S3 and S4). We refer to this mean circulation, driven by the top boundary temperature gradients, as horizontal convection [25]. In addition to horizontal convection, the internal dynamics of a lava planet is characterized by vertical convection driven by the temperature difference between the surface and the iron core. Although the temperature difference between the sub-stellar point and the CMB might be locally sub-critical with regards to thermal convection, the low temperature of the night-side ensures that the magma ocean is always globally thermally unstable. This vertical convection manifests itself as hot plumes forming at the CMB in our 3D and 2D simulations (Fig. 1a and 1b).

For a low-viscosity global magma ocean, rotation could influence the dynamics [20–22] (Methods). The balance between buoyancy and Coriolis forces—so-called thermal wind balance—predicts radial flows to occur where the azimuthal temperature gradient is the largest [26, 27]. In a linear, inviscid regime, this would lead to a 90° longitudinal shift of the mean circulation with

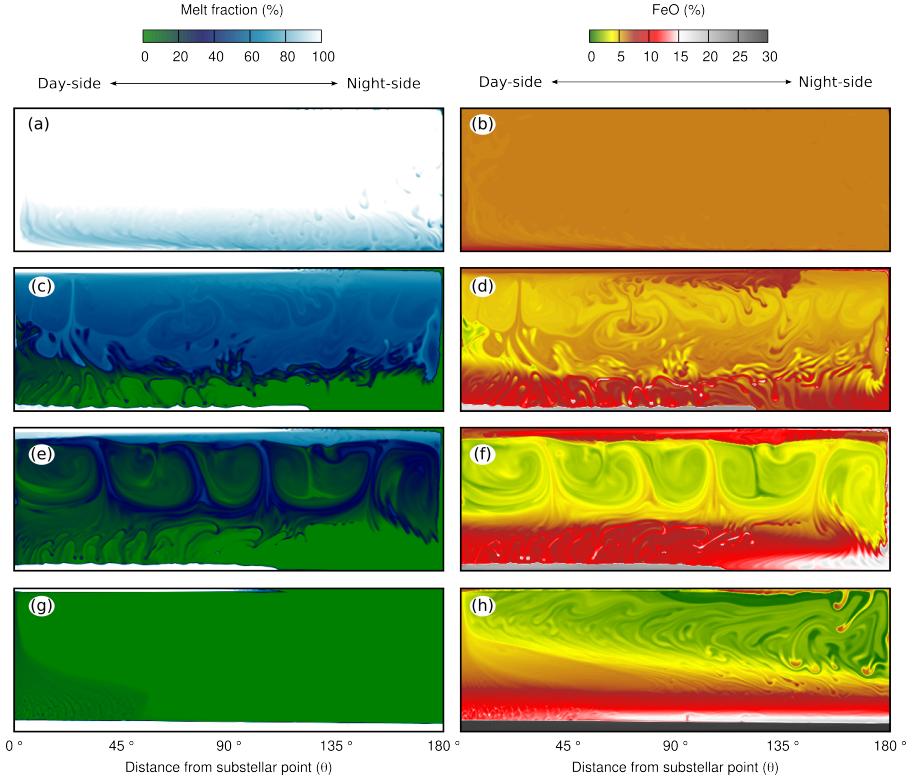
6 *Lava Planets Interior Dynamics*

Fig. 3 Compositional evolution of lava planets interiors from an initial homogeneous molten state. Chemical fractionation occurs during planetary solidification because rock-forming elements do not have the same affinities for liquid and solid phases. For instance, FeO prefers to remain in the liquid rather than being incorporated in the solids. (a and b) Initial conditions. The magma ocean is well mixed and nearly entirely molten. The composition of the magma ocean corresponds to the bulk planet’s composition, *i.e.*, 6% of FeO (BSE composition). This is the global magma ocean stage. (c and d) Onset of the mushy stage. The MO crystal fraction is about 50%. Iron-rich solids accumulate in the deep mantle. The most liquid part of the planet shows a FeO content of 10%. (e-f) End of the mushy stage. The FeO concentration of the MO reaches its maximum, 12%. (g-h) Solid-state stage. The iron-rich shallow magma ocean has been buried in the deep mantle. The day-side shallow magma ocean has a concentration of about about 2%. The solid mantle is strongly layered. Iron-rich solids remelts to form a basal magma ocean.

respect to the sub-stellar and anti-stellar point. Nonlinearities due to temperature advection and inertia, together with the development of strong zonal flows complicate this simple picture by contributing to shifting the downwelling currents, and by introducing an asymmetry between the warm and cold hemispheres (Fig. 2a-b and Supplementary Fig.S4). Note that the origin of this shift is *a priori* different from the atmospheric hotspot offsets predicted by shallow atmosphere models where equatorially trapped waves play a prominent role [28].

As the magma ocean cools we transition to 2D multiphase simulations, which can accommodate crystallization. Our 2D Cartesian approach when the

magma ocean is global lead to a qualitatively similar mean circulation, with downwelling on the night-side, and a global return flow on the day-side (SI Fig. S3). Our 3D spherical simulations confirm that even in the presence of 3D effects turbulence and rotation, this mean circulation pattern is robust, which validates our 2D Cartesian approach (SI Fig. S3).

The initial global magma ocean is compositionally homogeneous (Fig. 3a–b). Solidification increases the crystal fraction to the point where the silicate interior behaves more like a solid than a liquid; this rheological transition is expected to occur around 40% melt fraction [29]. Regions where the melt fraction ranges between 20% to 60% (where the shear viscosity of the solid-liquid mixture abruptly drops from about 10^{15} Pa s to 10^4 Pa s [30, 31]) are considered as being mushy. In our simulations, we observe that the mushy layer grows, and rapidly occupies the entire mantle. The cold temperature imposed at the night-side surface drives solidification as the temperature is below the solidus temperature of silicate rock, ~ 1000 K. However, this night-side crust is thermally and compositionally unstable: the night-side surface is colder than the interior, and solid silicates are denser than melt at ambient pressure. The night-side crust thus sinks as soon as it forms, and is constantly replaced by fresh and hot lava (links to movies are provided in the additional information section).

We define the onset of the mushy regime when the top of the mushy layer almost reaches the surface of the planet (Fig. 3c–d). Solids and liquids segregate, differentiating the planet (Fig. 3d) during the mushy regime. We model the chemical partitioning of FeO because it is the denser oxide and hence has the most important effect on the fluid dynamics of silicate solidification. FeO is also an anti-freeze agent that decreases the silicate solidification temperature. The FeO compositional fields depicted in Fig. 3 can be used as first-order proxies to anticipate the spatial partitioning of other species. FeO being an incompatible elements (*i.e.*, it prefers to remain in the melt rather than being incorporated in crystals), regions rich in FeO are expected to be enriched in other incompatible elements, whereas the FeO-poor regions will preferentially host compatible elements, such as MgO.

Upon solidification the magma ocean becomes enriched in FeO, which is incompatible. The day-side magma ocean composition increases up to 12 wt%—twice the value of Bulk Silicate Earth (BSE)—near the end of the intermediate regime (Fig. 3f). The FeO concentration can increase in the magma ocean as long as these FeO-rich silicates remain molten. However, horizontal convection moves these iron-rich liquids towards the night-side, where they solidify. FeO-rich solids are substantially denser than the average mantle and thus sink to the deep mantle. Consequently, the FeO-rich day-side magma ocean is progressively replaced by a FeO-poor magma ocean.

Lava planets enter their long-lasting solid-state regime when the average melt fraction of the mantle drops below 20% (Fig. 3e–f). The mantle is now compositionally stratified, affecting solid-state convection. Dense geochemical reservoirs may never be exposed to the surface. With a colder solidification

temperature than Mg-rich silicate, the FeO-rich lowermost mantle remelts (Fig. 3e–h), forming a basal magma ocean, as suggested for the Earth [32, 33], Mars [34] and Venus [35]. When the lava planet becomes essentially solid (Fig. 3g–h), the remaining day-side magma ocean is shallow, less than 200 km thick, because the cooling from the night-side has efficiently cooled the entire planet interior, not only its night-side hemisphere. This is also at odds with the results in [19] where heat transport between the two hemispheres of the planet was neglected. Even if the core is relatively hot (see Methods), a lava planet with no persistent heat sources will quickly and almost completely solidify.

Interior dynamics have a first-order control on the atmospheric pressure and composition. Indeed, several studies used melt-vapor equilibrium model to predict the composition, dynamics, and spectral characteristics of lava planets atmospheres [11, 14, 15, 18, 36, 37]. These approaches generally assume that the magma has the composition of the bulk silicate portion of the planet. As a working hypothesis, they further assume that the mantle has a BSE composition. However, these studies all noted that the magma ocean composition is in fact expected to differ from that of the BSE because (1) the host star composition is not necessarily Solar, and (2) the magma ocean composition can evolve with time due to both liquid–vapor fractionation at the surface of the planet, and solid–liquid fractionation in the planetary interiors. In this study, we investigate the issue of the internal solid-liquid fractionation that has not been addressed in previously. We are interested in the long-term, *i.e.*, billions years timescale, evolution of lava planets from an initial hot fully molten state to a final essentially solid-state stage.

Rock-forming elements such as Mg, Si, Na, or Fe have different affinities for solid rocks and silicate melts leading to chemical fractionation. Several elements prefer to remain in the melt as it is difficult for them to enter the crystallographic structure of solid rocks. Starting from a fully molten state, the concentration of these incompatible elements in a magma ocean increases upon solidification. Solid-liquid segregation must be faster than magma ocean solidification such that silicate fractionation can occur [20, 23, 24]. If magma ocean solidification is faster than solid–liquid segregation, as hypothesised to have been a relevant scenario in the Solar System, then the magma ocean freezes out as a homogeneous silicate layer. On a lava planet with a permanent day-side magma ocean, we expect long-term chemical fractionation of the magma ocean because gaseous, liquid and solid silicates are in contact for billions of years.

Lava planets have been identified as target of interest to be observed with JWST: with five different programs aiming at detecting and to observing lava planets [38–41]. Given their short orbital periods, lava planets are particularly amenable to full-orbit phase-resolved spectroscopy. In the light of our results, we postulate two observable end-member regimes for lava planets: either a hot,

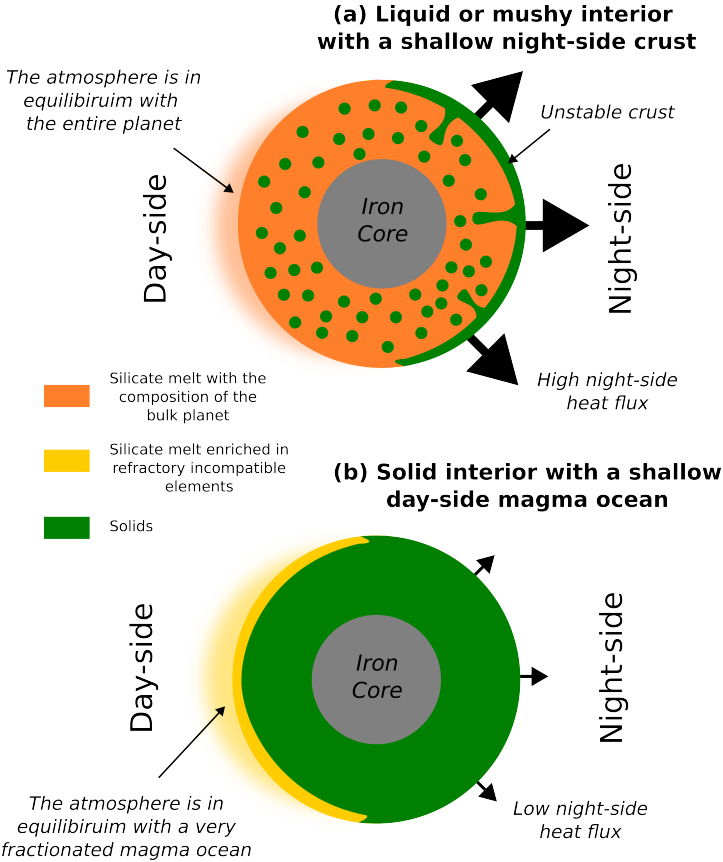


Fig. 4 Hot *vs.* cold end-member regimes of lava planet interiors. (a) The hot regime is characterized by an essentially liquid interior (orange). The hot regime can be observed at present-day either if the lava planet is very young or if tidal dissipation sustains a hot interior since its formation. Vigorous liquid-state convection favors compositional mixing and efficient cooling by heat transfer from the day-side to the night-side hemisphere. (b) The cold regime is characterized by a solid interior (green) with a shallow day-side magma ocean. Old lava planets with no tidal heating are expected to be in the cold regime. Continuous solid-liquid segregation has fractionated the magma ocean composition (yellow). Solid-state convection is too weak to generate an observable thermal signature on the night-side surface.

homogeneous global magma ocean regime, or a cold, chemically differentiated solid-state regime (Fig. 4).

The hot and cold regimes can be distinguished by measuring the day-side and night-side emission spectra of a lava planet. In the hot-interior scenario, the magma ocean and its overlying atmosphere reflect the bulk silicate composition of the planet, so we expect emission spectroscopy to reveal Na, K and FeO, in addition to the ubiquitous SiO [36]. On the other hand, if the planet's interior has mostly solidified, we expect relatively volatile Na and K to be locked on the night-side and FeO to be stuck in the deep mantle, leading to an atmosphere that will only exhibit SiO spectral features.

Moreover, if the magma ocean interior is hot and mostly molten, the night-side is expected to radiate at a high temperature. The unstable gravitational crust is constantly replenished by hot lava that radiate at about 1500 K before solidifying and being replaced. If the magma ocean extent is global, the heat flux coming from the interior due to vertical convection is expected to be very high, *i.e.*, larger than 10^3 W m^{-2} , and it could be as large as 10^6 W m^{-2} [20, 42]. Similar values are obtained using scaling laws relevant for horizontal convection [25]. Endogenic heat fluxes of 10^3 W m^{-2} and 10^6 W m^{-2} correspond to a night-side surface temperature of 900 K and 3000 K, respectively. A hot night-side surface temperature of a lava planet is an univocal signature of a hot internal state of the planet. Conversely, a very viscous solid interior cannot advect significant heat to the night-side, resulting in associated temperatures of the order of 100 K [12].

The interior present-day thermal state of planets is one of the most fundamental aspect of planetary evolution because it reflects the entire history of the planet since its formation. Therefore, probing the thermal state of planet offers precious information on its evolutionary path. For example, if a lava planet orbiting a 10 Gyrs-old star is found to be in the hot interior state, it would suggest that the interior is being tidally heated, presumably due to orbital interactions with companion planets. The intermediate regime described in this study may be extended in time due to tidal heating. Indeed, tidal dissipation is expected to be maximized in the partially molten regions [43], and thus reheat and remelt the planet. However, when the planet becomes entirely molten, tidal heating is probably small and cooling is expected to be rapid, bringing back the planetary interior in a partially molten state.

This study shows that a long-lived, shallow day-side magma ocean experiences solid-liquid chemical fractionation. In this case, the silicate atmosphere of the lava planet is expected to be in equilibrium with a highly fractionated magma ocean. This motivates a better understanding of silicate petrology for non-BSE composition - Is elemental affinity for solid and molten rocks applicable beyond Earth BSE-like compositions? Answering this question will allow to better identify elemental ratio that (1) tracks the compositional fractionation of the magma ocean, and (2) are detectable with spectroscopic methods.

Methods

2D multiphase flow model

We model the solid-liquid multiphase flow dynamics using the code **Bambari** [44]. The code implements the multiphase flow mathematical formalism based on the averaging method [44–48]. The original implementation [49, 50] was considerably improved in recent years, in particular with the use of the numerical stencils implemented for the momentum conservation in the Finite-Volume code **StreamV** [51, 52]. The latter allow handling reliably large and sharp viscosity contrasts with negligible spurious pressure effects [53]. We have also

extended the model of [44] from two to four phases to capture chemical fractionation between liquid and solid during phase change. Our model is composed of two mechanical phases: a liquid phase and a solid phase. Each mechanical phase is composed of two compositional phases that correspond to a FeO-rich end member and a MgO-rich end member. Density contrast between liquid and solid are described by two dimensionless buoyancy numbers in this new implementation (instead of only one in the former version of [44]). One buoyancy number is associated to the density difference between melt and solid of same chemical composition. The second buoyancy number describes the effect of composition, *i.e.*, FeO content, on density. Both buoyancy numbers are depth-dependent and parameterized based on a self-consistent thermodynamic model of [33] (see supplements).

On an discretized domain, solving the momentum conservation equation for the two mechanical phases involves the inversion of two sparse matrices, which are the most time-consuming operations. In **Bambari**, these matrix inversions are performed using the direct PARDISO library that is parallelized using **OpenMP** directives [54, 55]. We parameterize the mantle melting relations using a idealized binary loop that is fitted on high-pressure diamond anvil-cell experiments (see supplements). We use a Cartesian grid resolution of 200×600 square cells (aspect ratio is 3:1). The maximum thermal Rayleigh - that would characterize the convective vigor if the numerical domain was fully molten - is 10^9 . The viscosity contrast between melt and solid is 10^3 . Both surface and bottom temperature are imposed and constant. The surface temperature follows the gradient temperature imposed by stellar radiation [14]. Mechanical boundary conditions are free-slip on the four sides of the domain.

For phase change, we assume thermodynamic equilibrium between solid and liquid at every time-step, everywhere in the numerical domain. Phase change is thus not limited by reaction kinetics but only by phase diagram (that describes the solid-liquid equilibrium) and energy conservation (see supplements, Fig. S2) [56].

In Supplementary Table S1, we report typical estimates of magma oceans physical parameters and associated dimensionless parameters used in the 2D Cartesian simulations.

3D turbulent flow model

In the fully-molten, low viscosity case, we numerically model the magma ocean circulation by solving for turbulent thermal convection in a rotating spherical shell using the open-source code **MagIC** [57–59]. We solve the Navier-Stokes, mass conservation and energy conservation equations in spherical coordinates under the Boussinesq approximation [60]. Consistently with the 2D multiphase flow model, we use free-slip velocity boundary conditions at the bottom and at the top of the ocean. At the bottom surface the temperature is fixed to T_{bot} . We impose a heterogeneous temperature field at the top of the ocean to

represent the day-side and the night-side of the planet:

$$T_{\text{top}}(\theta, \phi) = T_0(1 + \gamma Y_1^1(\theta, \phi)), \quad (1)$$

where $Y_1^1(\theta, \phi) = -1/2\sqrt{3/2\pi}\sin(\theta)\cos(\phi)$ is the hemispheric spherical harmonic, θ is the colatitude ($\theta \in [0, \pi]$) ϕ is the longitude ($\phi \in [0, 2\pi]$) and T_0 is the average top temperature. To be consistent with the 2D model, γ is chosen such that the hottest temperature, at the sub-stellar point, is equal to the temperature at the bottom of the ocean. In **MagIC**, with Dirichlet boundary conditions, the average temperature jump $\Delta T = T_{\text{bot}} - T_0$ is used as the temperature scale, and the top and bottom dimensionless temperatures are set to $-r_i^2/(r_i^2 + r_o^2)$ and $r_o^2/(r_i^2 + r_o^2)$ respectively. In our case, $r_i/r_o = 0.5$ and $r_o - r_i = D = 1$, leading to $T_{\text{bot}} = 0.8$, $T_0 = -0.2$ and the temperature at the outer boundary varies between $T_{\text{top}}^{\text{max}} = 0.8$ at the sub-stellar point and $T_{\text{top}}^{\text{min}} = -1.2$ at the anti-stellar point.

The system is governed by three dimensionless parameters, the thermal Rayleigh number Ra (buoyancy/diffusion), the Ekman number E (viscosity/rotation) and the Prandtl number Pr (viscosity/thermal diffusivity). In addition, the bulk convective Rossby number Ro_c is a useful proxy to qualitatively assess the rotation influence on the convective flow [61]. In a slowly-rotating regime, it compares the free-fall time of a fluid parcel with a rotation period [62]:

$$Ro_c = \frac{U_{\text{ff}}}{\Omega D} = \frac{\sqrt{\alpha g_0 \Delta T D}}{\Omega D} = \frac{Ra^{1/2} E}{Pr^{1/2}},$$

where U_{ff} is the convective free-fall velocity, g_0 is the gravitational acceleration, α is the thermal expansivity, D is the thickness of the magma ocean, rotating at a rate Ω about the vertical axis z . In Supplementary Table S2, we report typical estimates of magma oceans physical parameters and associated dimensionless parameters. In a low-viscosity scenario, we obtain Ro_c in a range 1.4 – 7.6 (Supplementary Table S2). Since the Rossby number could reach values of order one, rotational effects, through the Coriolis force, can be as important as buoyancy effects. Therefore, we argue that both non-rotating and rotating regimes should be considered. Since realistic dimensionless parameters are out-of-reach with current computational capabilities, we work at more moderate Ekman and Rayleigh numbers, chosen such that the convective Rossby number remains of order one ($Pr = 1$, $Ra = 1.1 \times 10^8$, $E = 1.5 \times 10^{-4}$ and $Ro_c = 1.6$). This ensures the right force balance between buoyancy and rotation. For the non-rotating simulations, the Prandtl and Rayleigh are left unchanged and the Ekman number becomes irrelevant (*i.e.*, $E \rightarrow \infty$, $Ro_c \rightarrow \infty$).

MagIC employs a pseudo-spectral method with Chebyshev polynomials in the radial direction and spherical harmonics in the longitudinal and latitudinal directions, and the fast spherical harmonic transform library is used **SHTns** [59]. The simulations are ran with 201 grid points in radius, 1792 grid points in longitude and 896 in latitude. The equations are advanced in time using

a mixed time stepping scheme (Crank-Nicolson for the implicit terms and a second-order Adams-Bashforth for the explicit terms). The simulations were ran for 350 and 600 turnover times for the non-rotating and rotating simulations respectively, ensuring temporal convergence. For further details on the numerical methods, we refer the reader to code documentation (available at <https://magic-sph.github.io/>). MagIC is parallelized using both OpenMP (<http://openmp.org/wp/>) and MPI (<http://www.open-mpi.org/>) and the simulations were performed on the *Lonestar6* nodes of TACC supercomputer (<http://www.tacc.utexas.edu>).

References

- [1] Léger, A. *et al.* Transiting exoplanets from the corot space mission * - viii. corot-7b: the first super-earth with measured radius. *A&A* **506** (1), 287–302 (2009). URL <https://doi.org/10.1051/0004-6361/200911933>. <https://doi.org/10.1051/0004-6361/200911933> .
- [2] Batalha, N. M. *et al.* Kepler’s first rocky planet: Kepler-10b. *The Astrophysical Journal* **729** (1), 27 (2011). URL <http://stacks.iop.org/0004-637X/729/i=1/a=27> .
- [3] Sanchis-Ojeda, R. *et al.* Transits and Occultations of an Earth-sized Planet in an 8.5 hr Orbit. *The Astrophysical Journal Letters* **774** (1), 54 (2013). <https://doi.org/10.1088/0004-637X/774/1/54>, arXiv:1305.4180 [astro-ph.EP].
- [4] Vanderburg, A. *et al.* Two Small Planets Transiting HD 3167. *Astrophysical Journal* **829** (1), L9 (2016). <https://doi.org/10.3847/2041-8205/829/1/L9>, arXiv:1607.05248 [astro-ph.EP].
- [5] Barragán, O. *et al.* K2-141 b. A 5- M_{\oplus} super-Earth transiting a K7 V star every 6.7 h. *Astronomy and Astrophysics* **612**, A95 (2018). <https://doi.org/10.1051/0004-6361/201732217>, arXiv:1711.02097 [astro-ph.EP].
- [6] Malavolta, L. *et al.* An Ultra-short Period Rocky Super-Earth with a Secondary Eclipse and a Neptune-like Companion around K2-141. *aj* **155** (3), 107 (2018). <https://doi.org/10.3847/1538-3881/aaa5b5>, arXiv:1801.03502 [astro-ph.EP].
- [7] Espinoza, N. *et al.* HD 213885b: a transiting 1-d-period super-Earth with an Earth-like composition around a bright ($V = 7.9$) star unveiled by TESS. *Monthly Notices of the Royal Astronomical Society* **491** (2), 2982–2999 (2020). <https://doi.org/10.1093/mnras/stz3150>, arXiv:1903.07694 [astro-ph.EP].
- [8] Murgas, F. *et al.* HD 20329b: An ultra-short-period planet around a solar-type star found by TESS. *Astronomy and Astrophysics* **668**, A158

- (2022). <https://doi.org/10.1051/0004-6361/202244459>, arXiv:2211.02547 [astro-ph.EP].
- [9] Valencia, D., Ikoma, M., Guillot, T. & Nettelmann, N. Composition and fate of short-period super-earths-the case of corot-7b. *Astronomy & Astrophysics* **516**, A20 (2010) .
- [10] Schaefer, L. & Fegley Jr, B. Outgassing of ordinary chondritic material and some of its implications for the chemistry of asteroids, planets, and satellites. *Icarus* **186** (2), 462–483 (2007) .
- [11] Castan, T. & Menou, K. Atmospheres of hot super-earths. *The Astrophysical Journal Letters* **743** (2), L36 (2011) .
- [12] Kite, E. S., Fegley Jr, B., Schaefer, L. & Gaidos, E. Atmosphere-interior exchange on hot, rocky exoplanets. *The Astrophysical Journal* **828** (2), 80 (2016) .
- [13] Ito, Y. *et al.* Theoretical emission spectra of atmospheres of hot rocky super-earths. *The Astrophysical Journal* **801** (2), 144 (2015) .
- [14] Nguyen, T. G., Cowan, N. B., Banerjee, A. & Moores, J. E. Modelling the atmosphere of lava planet k2-141b: implications for low-and high-resolution spectroscopy. *Monthly Notices of the Royal Astronomical Society* **499** (4), 4605–4612 (2020) .
- [15] Nguyen, T. G., Cowan, N. B., Pierrehumbert, R. T., Lupu, R. E. & Moores, J. E. The impact of ultraviolet heating and cooling on the dynamics and observability of lava planet atmospheres. *Monthly Notices of the Royal Astronomical Society* **513** (4), 6125–6133 (2022) .
- [16] Zilinskas, M. *et al.* Observability of evaporating lava worlds. *Astronomy & Astrophysics* **661**, A126 (2022) .
- [17] Gelman, S., Elkins-Tanton, L. & Seager, S. Effects of stellar flux on tidally locked terrestrial planets: degree-1 mantle convection and local magma ponds. *The Astrophysical Journal* **735** (2), 72 (2011) .
- [18] Miguel, Y., Kaltenegger, L., Fegley, B. & Schaefer, L. Compositions of hot super-earth atmospheres: exploring kepler candidates. *The Astrophysical Journal Letters* **742** (2), L19 (2011) .
- [19] Boukaré, C.-É., Cowan, N. B. & Badro, J. Deep two-phase, hemispherical magma oceans on lava planets. *arXiv preprint arXiv:2205.02864* (2022) .
- [20] Solomatov, V. S. in *9.04 - magma oceans and primordial mantle differentiation* (ed.Schubert, G.) *Treatise on Geophysics* 91 – 119 (Elsevier,

- Amsterdam, 2007). URL <http://www.sciencedirect.com/science/article/pii/B9780444527486001413>.
- [21] Maas, C. & Hansen, U. Effects of earth's rotation on the early differentiation of a terrestrial magma ocean. *Journal of Geophysical Research: Solid Earth* **120** (11), 7508–7525 (2015). URL <http://dx.doi.org/10.1002/2015JB012053>. <https://doi.org/10.1002/2015JB012053> .
- [22] Maas, C. & Hansen, U. Dynamics of a terrestrial magma ocean under planetary rotation: A study in spherical geometry. *Earth and Planetary Science Letters* **513**, 81–94 (2019) .
- [23] Elkins-Tanton, L. T. Magma oceans in the inner solar system. *Annu. Rev. Earth Planet. Sci.* **40**, 113–139 (2012). <https://doi.org/10.1146/annurev-earth-042711-105503> .
- [24] Chao, K.-H. *et al.* Lava worlds: From early earth to exoplanets. *Geochemistry* **81** (2), 125735 (2021) .
- [25] Hughes, G. O. & Griffiths, R. W. Horizontal convection. *Annu. Rev. Fluid Mech.* **40**, 185–208 (2008) .
- [26] Zhang, K. & Gubbins, D. On convection in the earth's core driven by lateral temperature variations in the lower mantle. *Geophysical journal international* **108** (1), 247–255 (1992) .
- [27] Dietrich, W., Hori, K. & Wicht, J. Core flows and heat transfer induced by inhomogeneous cooling with sub-and supercritical convection. *Physics of the Earth and Planetary Interiors* **251**, 36–51 (2016) .
- [28] Showman, A. P. & Polvani, L. M. Equatorial superrotation on tidally locked exoplanets. *The Astrophysical Journal* **738** (1), 71 (2011) .
- [29] Lejeune, A.-M. & Richet, P. Rheology of crystal-bearing silicate melts: An experimental study at high viscosities. *Journal of Geophysical Research* **100**, 4215–4229 (1995) .
- [30] Costa, A. Viscosity of high crystal content melts: dependence on solid fraction. *Geophys. Res. Lett.* **32** (22) (2005) .
- [31] Costa, A., Caricchi, L. & Bagdassarov, N. A model for the rheology of particle-bearing suspensions and partially molten rocks. *Geochemistry, Geophysics, Geosystems* **10** (3) (2009) .
- [32] Labrosse, S., Hernlund, J. & Coltice, N. A crystallizing dense magma ocean at the base of the Earth's mantle. *Nature* **450** (7171), 866–869 (2007). URL <http://www.nature.com/nature/journal/v450/n7171/full/>

nature06355.html. <https://doi.org/10.1038/nature06355> .

- [33] Boukaré, C.-E., Ricard, Y. & Fiquet, G. Thermodynamics of the MgO-FeO-SiO₂ system up to 140 GPa: Application to the crystallization of Earth's magma ocean. *J Geophys. Res.: Solid Earth* **120** (9), 6085–6101 (2015). URL <http://dx.doi.org/10.1002/2015JB011929>. <https://doi.org/10.1002/2015JB011929>, 2015JB011929 .
- [34] Samuel, H. *et al.* The thermo-chemical evolution of mars with a strongly stratified mantle. *Journal of Geophysical Research: Planets* **126** (4), e2020JE006613 (2021) .
- [35] O'Rourke, J. G. Venus: A thick basal magma ocean may exist today. *Geophysical Research Letters* **47** (4), e2019GL086126 (2020) .
- [36] Schaefer, L. & Fegley, B. Chemistry of silicate atmospheres of evaporating super-earths. *The Astrophysical Journal Letters* **703** (2), L113 (2009) .
- [37] Zilinskas, M., Miguel, Y., van Buchem, C. & Snellen, I. Observability of silicates in volatile atmospheres of super-earths and sub-neptunes: exploring the edge of the evaporation desert. *Astronomy & Astrophysics* **671** (2023) .
- [38] Hu, R. *et al.* Determining the atmospheric composition of the super-earth 55 cancri e. *JWST Proposal. Cycle 1* 1952 (2021) .
- [39] Brandeker, A. *et al.* Is it raining lava in the evening on 55 cancri e? *JWST Proposal. Cycle 1* 2084 (2021) .
- [40] Dang, L. *et al.* A hell of a phase curve: Mapping the surface and atmosphere of a lava planet k2-141b. *JWST Proposal. Cycle 1* 2347 (2021) .
- [41] Espinoza, N. *et al.* The first near-infrared spectroscopic phase-curve of a super-earth. *JWST Proposal. Cycle 1* 2159 (2021) .
- [42] Lebrun, T. *et al.* Thermal evolution of an early magma ocean in interaction with the atmosphere. *Journal of Geophysical Research: Planets* **118** (6), 1155–1176 (2013) .
- [43] Kervazo, M., Tobie, G., Choblet, G., Dumoulin, C. & Běhouňková, M. Inferring io's interior from tidal monitoring. *Icarus* **373**, 114737 (2022) .
- [44] Boukaré, C.-E. & Ricard, Y. Modeling phase separation and phase change for magma ocean solidification dynamics. *Geochemistry, Geophysics, Geosystems* **18** (9), 3385–3404 (2017) .

- [45] Drew, D. A. Averaged field equations for two-phase media. *Studies in Applied Mathematics* **50** (2), 133–166 (1971) .
- [46] Mckenzie, D. The generation and compaction of partially molten rock. *Journal of Petrology* **25** (3), 713–765 (1984) .
- [47] Bercovici, D., Ricard, Y. & Schubert, G. A two-phase model for compaction and damage: 1. general theory. *Journal of Geophysical Research: Solid Earth* **106** (B5), 8887–8906 (2001). URL <http://dx.doi.org/10.1029/2000JB900430>. <https://doi.org/10.1029/2000JB900430> .
- [48] Keller, T. & Suckale, J. A continuum model of multi-phase reactive transport in igneous systems. *Geophysical Journal International* **219** (1), 185–222 (2019) .
- [49] Šrámek, O., Ricard, Y. & Bercovici, D. Simultaneous melting and compaction in deformable two-phase media. *Geophysical Journal International* **168** (3), 964–982 (2007) .
- [50] Šrámek, O. *Modèle d'écoulement biphasé en sciences de la Terre: fusion partielle, compaction et différenciation*. Ph.D. thesis, Université de Lyon - Ecole Normale Supérieure, Lyon (2007).
- [51] Samuel, H. Time-domain parallelization for computational geodynamics. *g-cubed* (2012). Doi:10.1029/2011GC003905 .
- [52] Samuel, H. A deformable particle-in-cell method for advective transport in geodynamic modelling. *Geophysical Journal International* **214**, 1744–1773 (2018). Doi:10.1093/gji/ggy231 .
- [53] Samuel, H. & Evonuk, M. Modeling advection in geophysical flows with particle level sets. *g-cubed* **11** (Q08020) (2010). Doi 10.1029/2010GC003081 .
- [54] Alappat, C. *et al.* A recursive algebraic coloring technique for hardware-efficient symmetric sparse matrix-vector multiplication. *ACM Trans. Parallel Comput.* **7** (3) (2020). URL <https://doi.org/10.1145/3399732>. <https://doi.org/10.1145/3399732> .
- [55] Bollhöfer, M., Schenk, O., Janalik, R., Hamm, S. & Gullapalli, K. State-of-the-art sparse direct solvers. *Parallel Algorithms in Computational Science and Engineering* 3–33 (2020). URL <https://doi.org/10.1007/978-3-030-43736-7.1>. <https://doi.org/10.1007/978-3-030-43736-7.1> .
- [56] Wallner, H. & Schmeling, H. Numerical models of mantle lithosphere weakening, erosion and delamination induced by melt extraction and emplacement. *International Journal of Earth Sciences* **105** (6), 1741–1760

(2016) .

- [57] Wicht, J. Inner-core conductivity in numerical dynamo simulations. *Physics of the Earth and Planetary Interiors* **132** (4), 281–302 (2002) .
- [58] Christensen, U. R. *et al.* A numerical dynamo benchmark. *Physics of the Earth and Planetary Interiors* **128** (1-4), 25–34 (2001) .
- [59] Schaeffer, N. Efficient spherical harmonic transforms aimed at pseudospectral numerical simulations. *Geochemistry, Geophysics, Geosystems* **14** (3), 751–758 (2013) .
- [60] Gastine, T., Wicht, J. & Aubert, J. Scaling regimes in spherical shell rotating convection. *Journal of Fluid Mechanics* **808**, 690–732 (2016) .
- [61] Gilman, P. A. Nonlinear dynamics of boussinesq convection in a deep rotating spherical shell-i. *Geophysical & Astrophysical Fluid Dynamics* **8** (1), 93–135 (1977) .
- [62] Aurnou, J. M., Horn, S. & Julien, K. Connections between nonrotating, slowly rotating, and rapidly rotating turbulent convection transport scalings. *Physical Review Research* **2** (4), 043115 (2020). <https://doi.org/10.1103/PhysRevResearch.2.043115> .
- [63] Nabiei, F. *et al.* Investigating magma ocean solidification on earth through laser-heated diamond anvil cell experiments. *Geophysical Research Letters* e2021GL092446 (2021) .
- [64] Solomatov, V. S. in *Fluid Dynamics of a Terrestrial Magma Ocean* (eds Canup, R. M., Richter, K. & et al.) *Origin of the Earth and Moon* 323–338 (The University of Arizona Press, 2000).

Acknowledgments

This work has received funding from the European Research Council (ERC) under the European Union’s Horizon 2020 research and innovation program (grant agreement no. 101019965— SEPtIM). Parts of this work were supported by the UnivEarthS Labex program at Université de Paris and IPGP (ANR-10-LABX-0023 and ANR-11-IDEX-0005-02). Numerical computations were partly performed on the S-CAPAD/DANTE platform, IPGP, France.

Author contributions

Author 1: C.-E. Boukaré - Conceived and designed the analysis - Designed the numerical simulations - Performed the numerical simulations - Produced the figures - Wrote the manuscript. **Author 2: D. Lemasquier** Performed the numerical simulations - Produced the figures and analyzed the

data. **Author 3: N. Cowan** Conceived and designed the analysis - Wrote the manuscript. **Author 4: H. Samuel** Designed the numerical simulations - Revised the manuscript. **Author 5: J. Badro** Conceived the analysis - Revised the manuscript.

Additional information

Physical parameters used in the models can be found in the Supplementary Information.

Videos corresponding to Figure 3 can be found via the following links :

- Figure 1 : [Temperature and FeO fields](#),
- Figure 1 : [Temperature and melt fraction fields](#).

Supplementary information

Parametrization

We use the following parametrization for the solid-liquid isochemical density contrast shown in Figure 5,

$$R_p(z) = \frac{R_p^s - R_p^c}{1 - e^{-\gamma}} (e^{-\gamma z} - 1) + R_p^s, \quad (2)$$

where z is the dimensionless depth, $R_p^s = 11.53$, $R_p^c = 0.82$, and $\gamma = 6$. The subscripts s and c refer to the surface and core-mantle-boundary (CMB), respectively.

We use the following parametrization for the compositional density contrast, i.e., that quantifies the role of the FeO content on density, shown in Figure 5,

$$R_c(z) = R_c^s + z \times (R_c^c - R_c^s), \quad (3)$$

where z is the dimensionless depth, $R_c^s = 4.11$, $R_c^c = 12.35$.

The branches that describe the liquidus and solidus temperatures in the simplified phase diagram we use (Fig. 6) are parameterized as follows,

$$T_L(z) = T_{\text{FeO}}(z) + (T_{\text{MgO}}(z) - T_{\text{FeO}}(z)) (1 - x_l^m), \quad (4)$$

$$T_S(z) = T_{\text{FeO}}(z) + (T_{\text{MgO}}(z) - T_{\text{FeO}}(z)) (1 - x_s)^n \quad (5)$$

where T_L is the liquidus temperature, T_S is the solidus temperature, T_{MgO} and T_{FeO} are the melting temperature of the pure end-members, x_l is the composition of the liquid in FeO, x_s is the composition of the solid in FeO, m and n are constant that we used to adjust the shape of the loop. We assume that T_{FeO} and T_{MgO} vary linearly with depth. In the dimensionless form, we use $T_{\text{FeO}}^s = 0.31$, $T_{\text{FeO}}^c = 0.44$, $T_{\text{MgO}}^s = 0.57$, $T_{\text{MgO}}^c = 0.88$, $m = 1.7$, and $n = 1.1$.

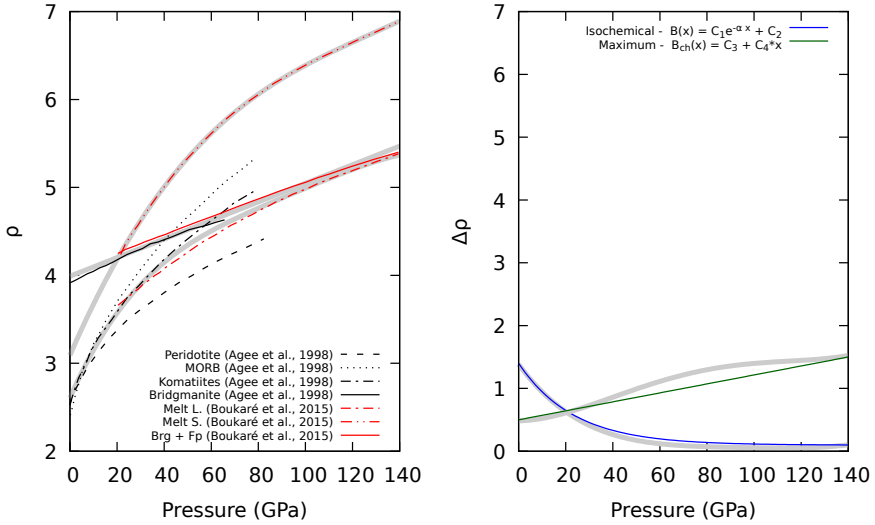


Fig. 5 Density contrast parametrization. (Left) Density of solid and liquid silicate as function of pressure for various composition. (Right) Density difference between solid and liquid. The thick grey lines correspond to the exact difference between the density curves shown on the left. The color lines depict the parametrization used in this study. The isochemical density contrast is shown in blue and captures to the effect of highest compressibility of silicate melt compared to their solid counterparts. The chemical density contrast corresponds to the density contrast between iron-rich and iron-free silicates.

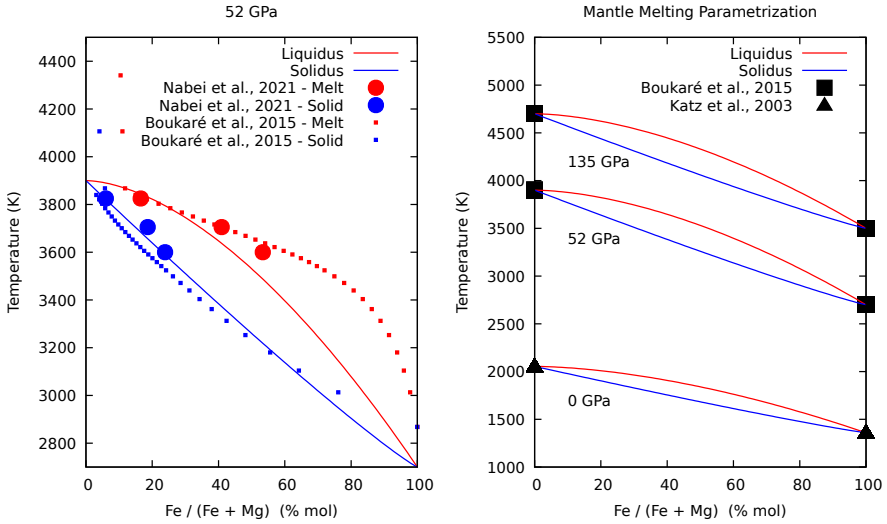


Fig. 6 Idealized binary loop model used to model solid-liquid melting relations in the Earth's mantle. This parameterization was obtained by fitting diamond anvil cell experiments [63] and self-consistent thermodynamic calculations [33].

Physical parameters

The physical parameters used in the 2D multiphase fluid dynamics simulations are listed in Tables 4. The physical parameters used in the 3D spherical simulations are listed in Table 2.

Comparison of 2D vs. 3D approaches

We use the 3D spherical simulations to validate our 2D Cartesian approach when the magma ocean is global. In particular, our 2D multiphase model considers an infinite Prandtl number dynamics, a regime representative of mantle-like convection with important viscous effects and negligible inertia. In the fully-molten period, if the viscosity of the fluid is low enough, finite Prandtl number dynamics becomes more relevant. Because of reduced viscous effects, the dynamics would be turbulent, and possibly affected by rotation, as suggested for the early Earth's magma ocean [21, 22]. Fig. 7 shows that even in the presence of rotation and turbulence, our 3D simulations confirm that the mean circulation pattern obtained in the 2D simulations is robust: a downwelling occur on the night-side, and a broad region of upwelling on the day-side. This degree-one pattern is reproduced in our 2D Cartesian simulations in the fully molten state before solidification starts.

DNS velocities

Parameters	Symbol (unit)	Value
Mean density	ρ_0 (kg m ⁻³)	4500
Depth-dependent isochemical density contrast	- (kg m ⁻³)	1400 – 100
Depth-dependent compositional density contrast	- (kg m ⁻³)	500 – 1500
Thermal expansivity	α_0 (K ⁻¹)	10 ⁻⁵
Gravity acceleration	g_0 (m s ⁻²)	9.81
Magma ocean thickness	D (km)	3000
Thermal diffusivity	κ (m ² s ⁻¹)	10 ⁻⁶
Thermal capacity	C_P (J K ⁻¹ kg ⁻¹)	1000
Latent heat of solidification	L (J kg ⁻¹)	1000
Solid viscosity	η_s (Pa s)	10 ²²
Liquid viscosity	η_l (Pa s)	10 ⁰
Compaction viscosity	η_b (Pa s)	10 ²²
Crystal size ¹	a (m)	10 ⁻⁶ -10 ⁻²
Surface temperature at the sub-stellar point	- (K)	2700
Surface temperature at the anti-stellar point	- (K)	0
Core temperature	- (K)	5000
Adiabatic temperature increase over the MO thickness	- (K)	1800
Maximum super adiabatic vertical temperature difference	ΔT_m (K)	2700
Maximum super adiabatic horizontal temperature difference	ΔT_h (K)	2700
Dimensionless parameters (Lava Planet)		
Solid-state Rayleigh	Ra	3.22×10^6
Liquid-state thermal Rayleigh	-	3.22×10^{28}
Solid-liquid viscosity contrast	-	10 ²²
Depth-dependent isochemical density contrast	R_p	11.15 – 0.823
Depth-dependent compositional density contrast	R_c	4.15 – 12.34
Stefan number	S_t	0.37
Melt mobility number ¹	δ	10 ¹ -10 ⁻³
Compaction viscosity	ζ	1
Dimensionless parameters (2D DNS)		
Solid-state Rayleigh	Ra	10 ⁶
Liquid-state Rayleigh	-	10 ⁹
Solid-liquid viscosity contrast	-	10 ³
Depth-dependent isochemical density contrast	R_p	11.15 – 0.823
Depth-dependent compositional density contrast	R_c	4.15 – 12.34
Stefan number	S_t	0.37
Melt mobility number ¹	δ	20×10^{-3}
Compaction viscosity	ζ	1

Table 1 Parameters used in the multiphase flow simulations. The momentum conservation equations associated to the dimensionless numbers can be found in [44]. Due to uncertainties associated to silicate melting temperature at extremely high pressure, *i.e.*, above 200 GPa, we consider here an Earth-sized lava planet. This choice prevents the use of arbitrary parameterization of melting curves and chemical density contrasts at more extreme pressures occurring in larger planets. ¹ Crystal size is captured by the dimensionless melt mobility number. A melt mobility number value of 20×10^{-3} for a Rayleigh number of 10^6 allows to explore a geodynamic regime where solid-liquid phase separation is efficient, generating a compositional evolution [44]). Dimensionless values are constrained by current computational limitations. For instance, a realistic solid-liquid viscosity contrast is currently out of reach in this kind of fluid dynamics simulations.

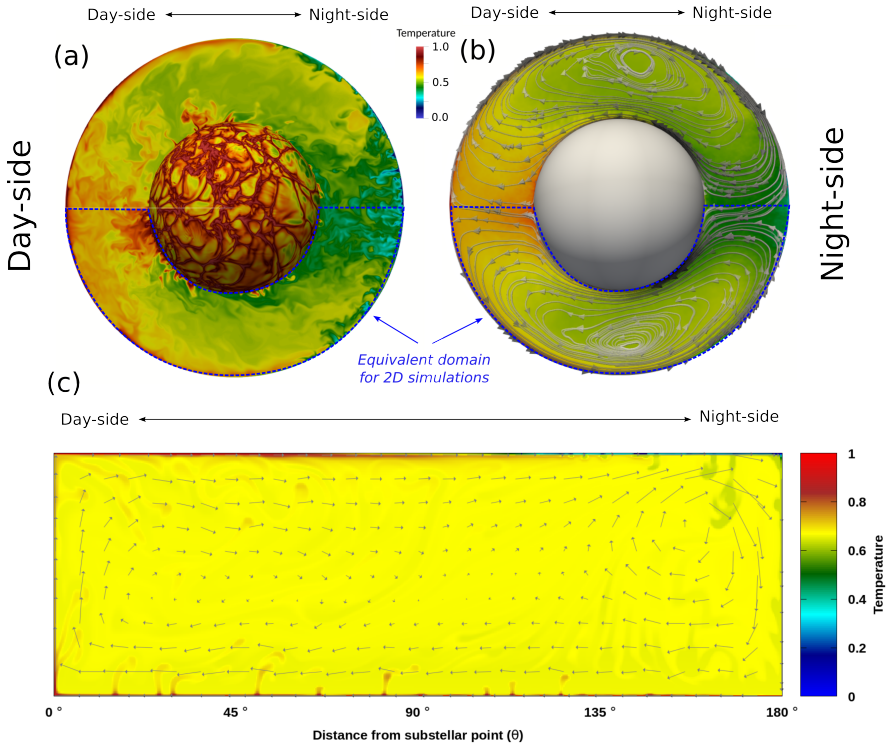


Fig. 7 Comparison of 2D Cartesian and 3D spherical simulations with no rotation. The temperature scale is the maximum super-adiabatic temperature contrast: temperature is 1 at the base of the magma ocean, 0 at the surface on the night-side and 1 at the surface on the day-side. (a) Snapshot of the temperature field in 3D spherical simulations. (b) Time-averaged temperature field and streamlines in the 3D spherical simulations. (c) Snapshot of the temperature field in the 2D Cartesian simulations.

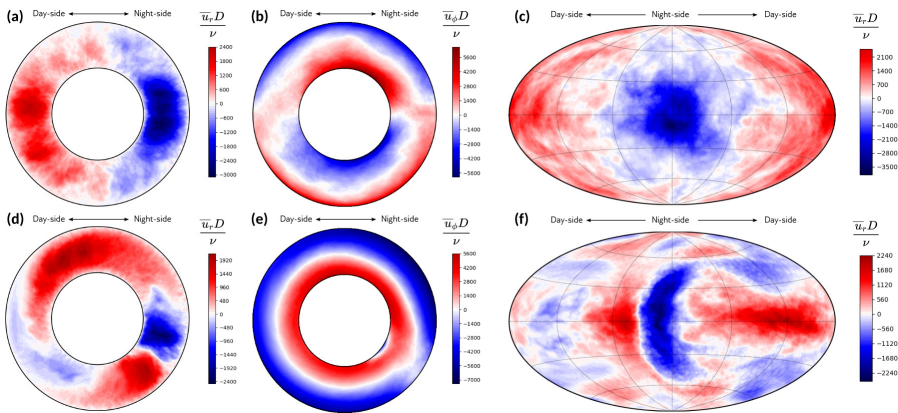


Fig. 8 Time-averaged radial (\overline{u}_r) and azimuthal (\overline{u}_ϕ) velocities in the DNS. (a-c) Non-rotating DNS. (d-f) Rotating DNS. (a,b,d,e) Equatorial planes. (c,f) Hammer projection of radial velocity at mid-depth in the magma ocean.

Parameters	Symbol (unit)	Value
Gravitational acceleration	g (m s^{-2})	20
Rotation period	T_Ω (hours)	6 to 18
Rotation rate	$\Omega = 2\pi/(T_\Omega \times 3600)$ (s^{-1})	9.7×10^{-5} to 2.9×10^{-4}
Magma ocean density	ρ (kg m^{-3})	8500
Dynamic viscosity ^a	η (Pa.s)	1×10^{-2}
Kinematic viscosity	$\nu = \eta/\rho$ ($\text{m}^2 \text{s}^{-1}$)	1.18×10^{-6}
Thermal diffusivity	κ ($\text{m}^2 \text{s}^{-1}$)	1×10^{-6}
Thermal expansion coefficient	α (K^{-1})	3×10^{-5} to 10×10^{-5}
Magma Ocean thickness	D (km)	5,000
Planet radius	r_o (km)	10,000
Average super-adiabatic vertical temperature difference	ΔT (K)	1350
Maximum super-adiabatic vertical temperature difference (Night-side)	ΔT_{max} (K)	2700
Minimum super-adiabatic vertical temperature difference (Day-side)	ΔT_{min} (K)	0
Dimensionless parameters (Lava Planet)		
Aspect ratio	$1 - D/r_o$	0.5
Prandtl ^a	$Pr = \nu/\kappa$	1.18
Rayleigh	$Ra = \alpha g \Delta T D^3 / (\nu \kappa)$	8.6×10^{31} to 2.9×10^{32}
Ekman	$E = \nu / (\Omega D^2)$	1.6×10^{-16} to 4.9×10^{-16}
Convective Rossby ^a	$Ro_c = \sqrt{Ra/PrE}$	1.4 to 7.6
Dimensionless parameters (3D DNS)		
Aspect ratio		0.5
Prandtl	Pr	1
Rayleigh	Ra	1.1×10^8
Ekman	E	∞ (non-rotating) 1.5×10^{-4} (rotating)
Convective Rossby	Ro_c	∞ (non-rotating) 1.6 (rotating)

Table 2 Physical parameters [2, 5, 64] for global magma oceans of lava planets and corresponding dimensionless parameters. Here, we assume a fully-molten, low-viscosity scenario (^a). Parameters range are considered to illustrate the sensitivity of the convective Rossby number. Dimensionless parameters used in the 3D Direct Numerical Simulations (DNS) are provided for comparison. Lava planets Rayleigh and Ekman numbers are out-of-reach of DNS, but a realistic convective Rossby number can be obtained to ensure a correct force balance between buoyancy and rotation. The rotating simulations fall in the transitional regime of Ref.[60].